ACS APPLIED MATERIALS & INTERFACES

Research Article

www.acsami.org

Polypyrrole-Supported Membrane Proteins for Bio-Inspired Ion Channels

Maria M. Pérez-Madrigal,[†,‡] Luis J. del Valle,[†] Elaine Armelin,[†,‡] Catherine Michaux,[§] Guillaume Roussel,[§] Eric A. Perpète,[§] and Carlos Alemán*[,†,‡]

[†]Departament d'Enginyeria Química, ETSEIB, Universitat Politècnica de Catalunya, Avda. Diagonal 647, Barcelona E-08028, Spain

[‡]Center for Research in Nano-Engineering, Universitat Politècnica de Catalunya, Campus Sud, Edifici C′, C/Pasqual i Vila s/n, Barcelona E-08028, Spain

[§]Unité de Chimie Physique Théorique et Structurale (UCPTS), University of Namur, Rue de Bruxelles, 61, 5000 Namur, Belgium

Supporting Information

ABSTRACT: Biomedical platforms constructed by immobilizing membrane proteins in matrixes made of synthetic organic polymers is a challenge because the structure and function of these proteins are affected by environmental conditions. In this work, an operative composite that regulates the diffusion of alkali ions has been prepared by functionalizing a supporting matrix made of poly(*N*-methylpyrrole) (PNMPy) with a β-barrel membrane protein (Omp2a) that forms channels and pores. The protein has been unequivocally identified in the composite, and its structure has been shown to remain unaltered. The PNMPy−Omp2a platform fulfills properties typically associated with functional bio-interfaces with biomedical applications (e.g., biocompatibility, biodegradability, and hydrophilicity). The functionality of the immobilized protein has been examined by studying the passive ion transport response in the presence of electrolytic solutions with Na^+ and K^+ concentrations close to those found in blood. Although the behavior of PNMPy and PNMPy−Omp2a is very similar for solutions with very low concentration, the resistance of the latter decreases drastically when the concentration of ions increases to ∼100 mM. This reduction reflects an enhanced ion exchange between the biocomposite and the electrolytic medium, which is not observed in PNMPy, evidencing that PNMPy−Omp2a is particularly well suited to prepare bioinspired channels and smart biosensors.

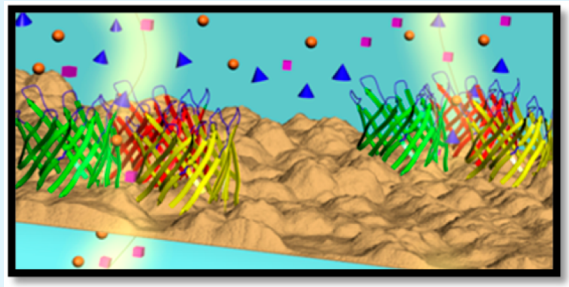

KEYWORDS: *bioinspired channels, electroactive polymer, electrochemical impedance spectroscopy, ion exchange, functional bio-interfaces*

INTRODUCTION

The development of hybrid surfaces made of synthetic polymers and biomolecules for biomedical applications has the potential to revolutionize the treatment of a wide variety of medical conditions. Due to their excellent electrochemical, chemical, and optical properties,[1−3] conjugated conducting polymers (CPs) are promising candidates for biomolecule immobilization and subsequent formation of one- and two-dimensional composites for biomedical devices (e.g., biosensors, electrochemical actuators, substrates for tissue engineering, and nanowires).[4−10]

On the other hand, biological membranes (lipid bilayers) are unique natural interfaces with exceptional solute transport selectivity and permeability properties, which are mainly due to the embedded membrane proteins (MPs). MPs participate in various cellular processes, such as signaling biochemical cascades, cell-to-cell communication, membrane fusion, and ion transport.[11,12] MPs play a central role in controlling a wide array of gradients such as chemical, electrical, and mechanical gradients and are responsible for cell structure during key events such as cellular division. Furthermore, many signal transduction processes between cells, such as neurons and muscle tissue, rely on the gating of ion channels (passive transport) and pumps (active transport), which allow the flow of ions across the biomembrane. In these processes, MPs act as channels that move specific molecules and ions into and out of the membrane, and their function is triggered by ligand binding or changes in the transmembrane potential.[13]

Considering that folding processes in MPs of lipid bilayers represent an important challenge in structural biology,[14,15] it is not surprising that the proper immobilization of purified MPs in platforms for biomedical applications, for example, micro- and nanoarrays, results in a very difficult task. Thus, drastic changes in natural environmental conditions affect MPs structure, influencing their activity.[16] In addition, the complex nature of proteins, their insolubility in aqueous solutions, and their instability in the presence of detergents strongly complicate the fabrication of protein-integrated devices based

Received: October 16, 2014
Accepted: December 25, 2014
Published: January 13, 2015

DOI: 10.1021/am507142f
ACS Appl. Mater. Interfaces 2015, 7, 1632−1643

on MPs. Despite these limitations and following biomimicking approaches, some advances have been reported using polymers as soft substrates,[17−25] even though only a few of them involved CPs.[24,25] In a recent study, Arun and Narayan[24] anchored bacteriorhodopsin, a MP that functions as a light-driven proton pump, onto conducting surfaces of poly(3,4-ethylenedioxythiophene) (PEDOT) and polyaniline (PAni). More recently, Della Pia et al.[25] used electropolymerization and amphipatic polymers to functionalize micro- and nanosurfaces with MPs. Specifically, these authors used gold surfaces selectively modified by electrogeneration of polypyrrole (PPy) in the presence of biotin, and the strong affinity of biotin for avidin was exploited to immobilize streptavidin proteins.[25] These hybrid platforms were proposed to be particularly suited to fabricate specific antibody bionanosensors. Because of these recent advances, composites combining CPs and MPs are expected to be functional materials with advanced properties and applications.

In this work, a CP−MP nanocomposite with regulated channeling activity has been prepared and characterized. The trimeric outer MP Omp2a from *Brucella melitensis*[26] has been selected for this purpose. This β-barrel protein forms pores that allow the diffusion not only of ions but also of molecules as large as 667 Da (e.g., nutrients and antibiotics). Indeed, pores are larger in Omp2a than in its homologue Omp2b (85% sequence identity and both encoded in the same genetic locus).[27] Although the function of Omp2a is still poorly understood at the structural level, as the 3D structure of Brucella β-barrel MPs is not known yet, very recent refolding studies suggested that Omp2a first refolds under a monomeric form and then self-associates into a trimeric state.[28,29] On the other hand, poly(*N*-methylpyrrole) (PNMPy) is the CP chosen to act as the supporting matrix for Omp2a. This PPy derivative displays a compact structure[30] and relatively infrequent formation of chemical cross-links when prepared under controlled conditions.[31] PNMPy has been successfully used in different biomedical and biotechnological applications, as for example the detection of glucose,[32] neurotransmitters,[6] and opioids.[33]

Herein, we describe the procedure to successfully prepare PNMPy-supported MP composites, and the characterization of their surface, electrochemical, and biomedical related properties. Subsequently, we demonstrate the potential of this new material to be used as electroactive stable synthetic membranes with enhanced ion permeability for biomedical applications by means of electrochemical impedance spectroscopy (EIS), and using different electrolytic solutions with K^+ and Na^+ concentrations similar to those found in blood. The observed passive ion transport properties indicate that PNMPy−Omp2a system is well suited for the preparation of smart bioinspired interfaces. Specifically, the ionic transport exerted by PNMPy−Omp2a has wide potential applications in nanofluidics, energy conversion, and biosensors.

METHODS

Experimental procedures related to the expression and purification of the trimeric Omp2a outer membrane protein from *Brucella melitensis*; the refolding of this protein; the synthesis of PNMPy and PNMPy−Omp2a films; and measurements such as thickness, cyclic voltammetry (CV), circular dichorism (CD), X-ray photoelectron spectroscopy (XPS), UV−vis spectroscopy, scanning electron microscopy (SEM), and atomic force microscopy (AFM) are described in the Supporting Information.

Wettability. Contact angle measurements were carried out using the water drop method. Images of 0.5 μL distillated water drops were recorded after stabilization with the equipment OCA 15EC (Data-Physics Instruments GmbH, Filderstadt). SCA20 software was used to analyze the images and determine the contact angle value, which was obtained as the average of at least six independent measures for each sample.

Enzymatic Degradation. PNMPy−Omp2a films were immersed in 1 mL of phosphate buffered saline solution (PBS) supplemented with 0.1 mg mL^{-1} of sodium azide (which allowed us to prevent contamination) and 50 μg mL^{-1} of Lipase F-AP15 to examine the enzymatic degradation of the protein. Incubation took place at 37 °C in a shaking incubator set at 100 rpm. Samples were analyzed after 1, 4, 8, 24, 48, and 72 h. After each immersion time, samples were removed from the solution and gently washed with distillated water. Then, samples were dried under vacuum for several days at room temperature before being observed by SEM.

Cellular Adhesion. Vero cells (African green monkey kidney epithelial cell line) and Cos-7 cells (African green monkey kidney fibroblast cell line) were cultured in Dulbecco's modified Eagle medium (DMEM) supplemented with 10% fetal bovine serum, 1% penicillin/streptomycin, and 2 mM L-glutamine at 37 °C in a humidified atmosphere of 5% CO_2 in air. The cultured medium was changed every 2 days, and for subculture, cell monolayers were rinsed with phosphate buffered saline (PBS) and detached by incubation with 0.25% trysin/EDTA for 5 min at 37 °C. Cell concentration was determined by counting at the Neubauer camera using 4% trypan blue as dye vital. The detached cells with viability ≥95% were used for cultures following the conditions for the adhesion assays.

PNMPy−Omp2a and PNMPy films deposited onto steel AISI 316 sheets of 1 cm^2 were placed in plates of 24 wells and sterilized using UV irradiation for 15 min in a laminar flux cabinet. Samples were incubated with 1 mL of culture medium during 30 min under culture conditions to equilibrate the material. Finally, the medium was aspired, and the material was evaluated for cell adhesion by exposing cells to direct contact with the material surface. An aliquot of 50 μL containing 5×10^4 cells was deposited on the substrate of each well. The plate was incubated under culture conditions for 60 min to promote the cell attachment to the film surface. Finally, 1 mL of the culture medium was added to each well. Controls of adhesion were simultaneously performed by culturing cells on the surface of the tissue culture polystyrene (TCPS) plates and uncoated steel. Cell adhesion was evaluated after 24 h of culture using the MTT [3-(4,5-dimethylthiazol-2-yl)-2,5-diphenyltetrazolium bromide] assay, which determines the cell viability. The viability results were normalized to TCPS control as relative percentages.

Results were derived from the average of four replicates ($n = 4$) for each independent experiment. ANOVA and Turkey tests were performed to determine the statistical significance, which was considered at a confidence level of 95% ($p < 0.05$).

Electrochemical Impedance Spectroscopy (EIS). Spectra were taken at open circuit potential (OCP) over the frequency range of 10 kHz−10 mHz with a potential amplitude of 0.05 V using an AUTOLAB-302N potentiostat/galvanostat. Typical potassium and sodium blood concentrations vary from 3.5 to 5.2 mM and 135 to 145 mM, respectively. Besides, K^+ is at a higher concentration in intracellular regions than outside the membrane by 2 orders of magnitude, whereas the opposite is true for Na^+ or Cl^- ions. Therefore, EIS spectra were collected using different aqueous electrolyte mediums at low and high ionic concentrations for KCl (5 and 100 mM) and NaCl (5 and 140 mM).

RESULTS AND DISCUSSION

Synthesis and Characterization of PNMPy−Omp2a. The Omp2a protein was expressed, purified, and refolded using the procedure described in the Methods section. The molecular weight and isoelectric point of trimeric Omp2a (367 amino acids) are 113.4 kDa and 4.47, respectively. PNMPy−Omp2a films were prepared by in situ anodic polymerization introducing Omp2a (1 mg mL^{-1}) in the generation medium, which consisted of a 15 mM monomer solution in deionized

DOI: 10.1021/am507142f
ACS Appl. Mater. Interfaces 2015, 7, 1632−1643

water with 10 mM of sodium dodecyl sulfate (SDS). Cyclic voltammograms recorded for the anodic oxidation of *N*-methylpyrrole (NMPy) monomer with and without the MP in the generation medium (ESI) reflected an anodic process with anodic peak potentials of 1.119 and 1.089 V, respectively. According to these results, PNMPy−Omp2a and PNMPy films were deposited onto steel AISI 316 sheets using a potential of 1.10 V and a polymerization time of 20 s. The thickness of PNMPy−Omp2a and PNMPy films, as determined by optical profilometry, is 219 ± 71 nm and 298 ± 72 nm, respectively.

The chemical composition of PNMPy−Omp2a composite was initially characterized by XPS, as shown in Table 1 and Figure 1. Spectra associated with control PNMPy are provided in the Supporting Information. As expected, the oxygen content in the atomic percent composition is higher for PNMPy−Omp2a than for PNMPy due to the presence of the MP (the protein sequence is displayed in the Supporting Information). Deconvolution of the high-resolution XPS spectrum in the C1s region for the composite led to three Gaussian curves that have been attributed to the saturated and conjugated C−C/C═C bonds[34,35] (284.5 eV) of NMPy units, the C═O bond (287.5 eV) of oxidized NMPy units[34,36] (i.e., N-substituted PPy derivatives typically undergo an oxidation process), and the C−N, C−NH_3^+, and C═O from peptide bonds (286.3 eV) in the protein.[37,38]

Table 1. Atomic and Mass Percent Composition of PNMPy and PNMPy−Omp2a

		C1s	N1s	O1s	S2p
PNMPy	atomic composition	70.7	7.9	18.9	2.5
	mass composition	63.3	8.3	22.5	5.9
PNMPy−Omp2a	atomic composition	53.9	3.6	39.4	3.1
	mass composition	45.4	3.5	44.2	6.9

The high-resolution N1s spectrum of control PNMPy (Supporting Information) shows two peaks centered at 399.9 eV (6.9%) and 401.4 eV (1.0%), which have been assigned to the C−N bonds of NMPy units involving neutral and charged nitrogen, respectively.[34,39] The ratio 1.0/(6.9 + 1.0) = 0.13 represents the fraction of charged nitrogen, which can be associated with the doping level of the electropolymerized material (Supporting Information). In contrast, PNMPy−Omp2a presents a single peak at 399.5 eV due to the overlapping of the binding energies associated with the C−N bond of NMPy units and the N−C═O (amide) of the protein, the latter being also around 400 eV.[37,40] The annihilation of the peak associated with the charged nitrogen atom indicates that the doping level of the CP in the composite is lower than that in the control, which is fully consistent with the low polymerization charge registered for the composite during the electrogeneration process. Furthermore, the absence of a peak at around 401.5 eV reflects that the amount of positively charged residues in Omp2a is very low.[37,38] Thus, Arg and Lys are essentially present in the composite as uncharged species, photoemitting at the same region that amides in high-resolution N1s spectra.

The high-resolution O1s spectra of both control PNMPy (Supporting Information) and PNMPy−Omp2a samples show three peaks. Those of PNMPy have been attributed to the sulfate groups of SDS (531.6 eV), the C═O of oxidized NMPy units (533.7 eV), and the metallic oxides on the steel substrate (529.1 eV). The $C/O_{531.6}$ and $N/O_{531.6}$ composition ratios, where C and N refer to the total compositions displayed in Table 1, and $O_{531.6}$ corresponds to the relative contribution to the total atomic O percent composition of the peak at 531.6 eV (Supporting Information), are 4.3 and 0.5, respectively. For

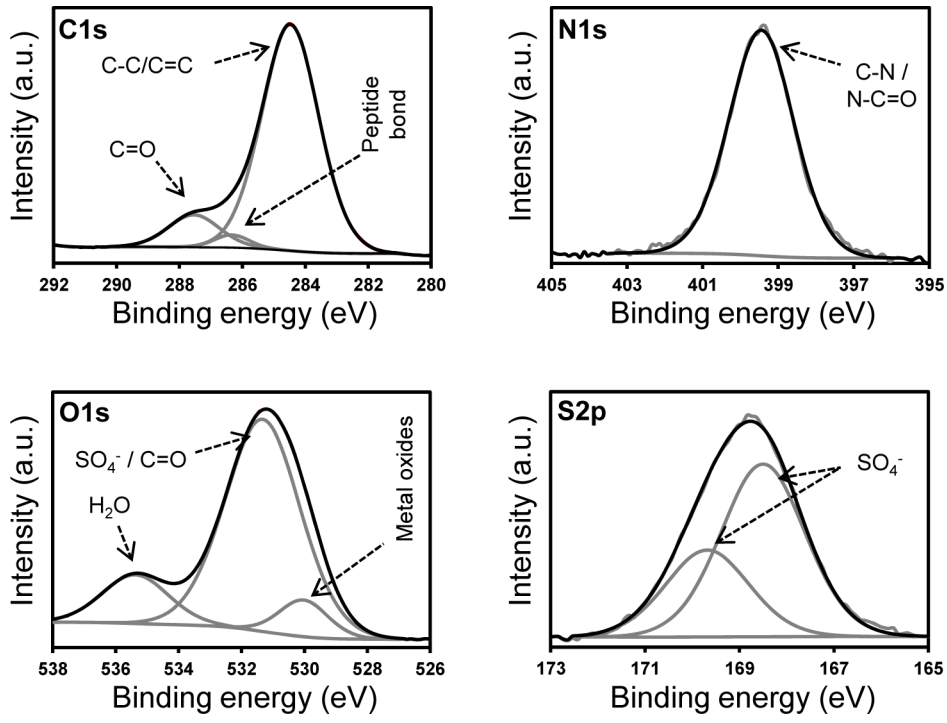

Figure 1. High-resolution C1s, N1s, O1s, and S2p XPS spectra for PNMPy−Omp2a. Peaks from deconvolution are also displayed (gray lines). Intensity is displayed in arbitrary units.

DOI: 10.1021/am507142f
ACS Appl. Mater. Interfaces 2015, 7, 1632−1643

PNMPy−Omp2a, the peaks detected in the high-resolution O1s spectra appear at 531.3, 535.4, and 530.0 eV. The first one involves not only the sulfate groups of SDS but also the C═O from the peptide bond.[37,38] Accordingly, the $C/O_{531.3}$ and $N/O_{531.3}$ ratios are 1.8 and 0.1, respectively, which are lower than in control PNMPy. The peak at 535.4 eV has been attributed to the water oxygen from moisture of the samples,[41,42] while the peak at 530.0 eV corresponds to metallic oxides at the substrate surface.

Finally, the S2p high resolution spectrum registered for PNMPy and PNMPy−Omp2a samples are very similar. Both show the spin-split sulfur coupling at 168.3 eV ($S2p_{3/2}$) and 169.5 eV ($S2p_{1/2}$), which is associated with the sulfate groups of the surfactant. Moreover, the S2p spectrum for PNMPy (Supporting Information) also present small peaks at 170.4 eV ($S2p_{3/2}$) and 171.5 eV ($S2p_{1/2}$), which correspond to metallic sulfates at the steel surface.

UV−vis absorption spectra were registered in the 200−350 nm range to further confirm the presence of Omp2a in the PNMPy−Omp2a composite, which was achieved by identifying the bands associated with the absorption of the peptide group and side groups of aromatic amino acids. PNMPy−Omp2a films were removed from the steel substrate and suspended in water to conduct the UV−vis measurements. Comparison recorded spectra, which are displayed in Figure 2, indicate

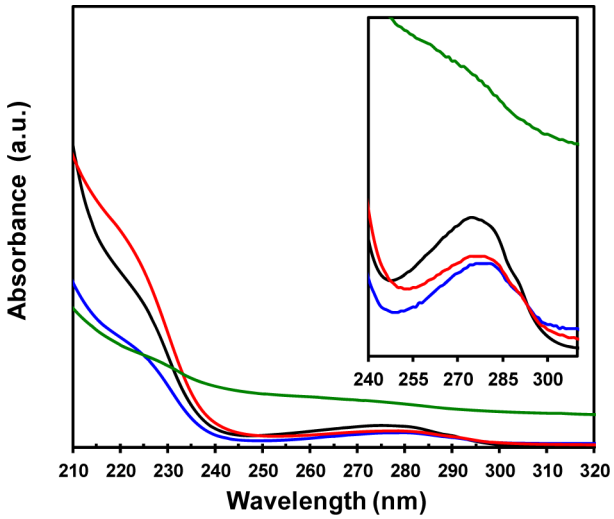

Figure 2. UV−vis spectra for as obtained (black) Omp2a, (blue) dialyzed Omp2a, (red) the Omp2a-containing polymerization medium, and (green) a PNMPy−Omp2a suspension.

typical absorptions of the peptide group and the aromatic side chains of tryptophan (Trp), tyrosine (Tyr), and phenylalanine (Phe) residues were detected as shoulders in the spectrum of PNMPy−Omp2a suspensions when compared to the spectra recorded for the control protein mediums (Figure 2). Thus, peptide groups typically absorb between 180 and 230 nm, while the aromatic side chains of Trp, Tyr, and Phe amino acids absorb in the 240−300 nm range.[43] Accordingly, spectra of as obtained Omp2a, dialyzed Omp2a and the Omp2a-containing polymerization medium show absorption maxima at such regions. More specifically, the shoulders detected at 289 and 260 nm come from the Trp (10 residues in Table S1, Supporting Information) and Phe (18 residues in Table S1, Supporting Information) residues, respectively.[43] The absorbance of the disulfide bond formed by the two Cys residues (Table S1, Supporting Information) at 260 nm also contributes to the latter shoulder. All these peaks appear as shoulders in the spectrum of PNMPy−Omp2a suspension. Protein absorbance was zero above 310 nm.

Although XPS and UV−vis results confirm the correct immobilization of Omp2a into the PNMPy matrix during the electrogeneration process, the native structure of the protein in the PNMPy−Omp2a composite was successfully corroborated by circular dichroism (CD) spectroscopy. Figure 3 compares

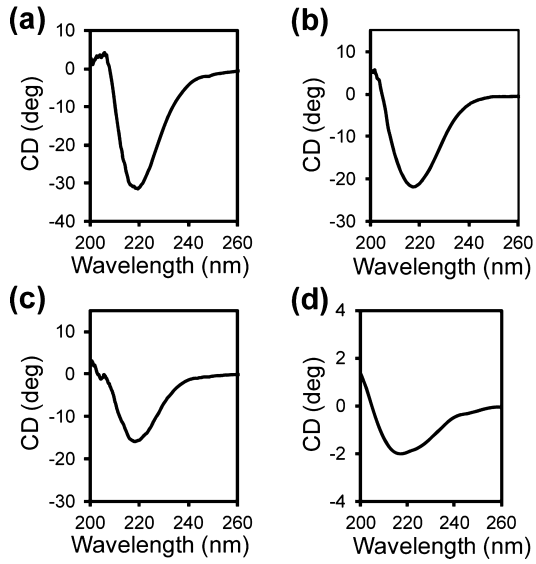

Figure 3. CD spectra for (a) as-obtained Omp2a, (b) dialyzed Omp2a, (c) Omp2a-containing polymerization medium, and (d) PNMPy−Omp2a composite. Protein concentration is 0.05 mg mL^{-1} in all cases with the exception of PNMPy−Omp2a composite.

the CD spectra for the expressed protein as obtained, after dialysis, and once incorporated into the NMPy-containing polymerization medium (Supporting Information). In all cases, the profile exhibits a band at ∼217 nm, which is typically found in β-stranded proteins.[44] This characteristic band is preserved in the CD spectra of the composite (Figure 3d), evidencing that the native β-sheet secondary structure is preserved when the pore-forming protein is immobilized into the polymeric matrix. Therefore, the operative and functional state of the PNMPy−Omp2a interface is ensured by having the MP Omp2a in its folded and/or assembled form.

On the other hand, the UV−vis absorption spectra of steel-supported control PNMPy and PNMPy−Omp2a films (Figure 4) indicate that the protein affects the oxidation process of the CP during the electrochemical polymerization, as it has already been mentioned. The first absorption band corresponds to the $\pi-\pi^*$ transition of aromatic rings (λ_{max} = 338 and 377 nm for PNMPy and PNMPy−Omp2a, respectively). The band gap energy, which was determined from the onset wavelength,[45] is 2.44 and 2.30 eV for PNMPy and PNMPy−Omp2a, respectively. The second absorption band is related to the first stages of the oxidation process and has been assigned to the formation of polarons. This band is clearly defined for PNMPy at λ_{max} = 567 nm, whereas for PNMPy−Omp2a samples this oxidation process is only identified as a weak shoulder at ∼565 nm in the UV−vis spectrum. This feature is fully consistent with XPS results, which suggested that the doping level of the composite was lower than that of PNMPy.

DOI: 10.1021/am507142f
ACS Appl. Mater. Interfaces 2015, 7, 1632−1643

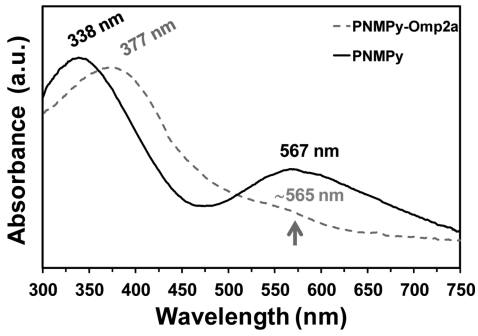

Figure 4. UV−vis spectra for control PNMPy and PNMPy−Omp2a films deposited onto steel sheets. The values of λ_{max} are indicated.

Neither system displays an absorption band in the range of 650−700 nm, which is typically assigned to very high oxidation levels (bipolaric states).[36]

Surface Properties. To better understand the passive ion transport response of PNMPy−Omp2a composite, its surface properties were evaluated.

Surface morphology and topography of PNMPy−Omp2a were deeply examined by SEM and AFM, respectively. Control PNMPy films (Figure 5) show a very compact and dense

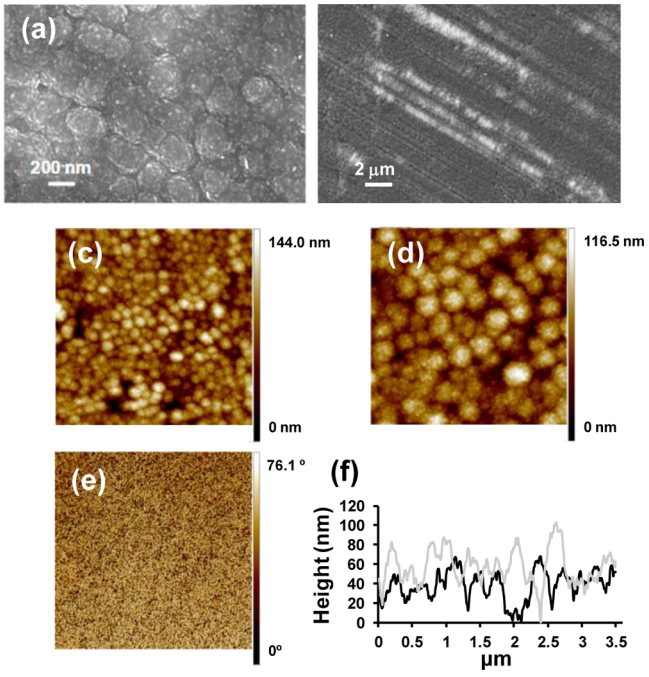

Figure 5. PNMPy surface characterization: SEM micrograph at (a) 100 and (b) 10 kX; (c) 5.0 × 5.0 and (d) 2.5 × 2.5 μm AFM height images; (e) 2.5 × 2.5 μm^2 AFM phase image corresponding to image d; and (f) cross-sectional profiles obtained from image d. In the cross-sectional profiles, the black line corresponds to the diagonal drawn from the lower left corner to the upper right corner, while the gray line corresponds to the diagonal drawn from the upper left corner to the lower right corner.

globular structure that is consistent with a homogeneous distribution of the polymer chains. RMS roughness of PNMPy (23 ± 9 nm) is similar to that of steel substrate (18 ± 5 nm). These features indicate a multidirectional growing of polymers that is only possible through the formation of some chemical couplings involving the β- and β'-positions of the repeat units. Accordingly, the transport of ions through this partially cross-linked polymeric matrix is expected to be hindered by the densely packed structure.

Incorporation of the protein provokes significant changes in the surface morphology. SEM micrographs and AFM height images of PNMPy−Omp2 (Figure 6) show elements of both

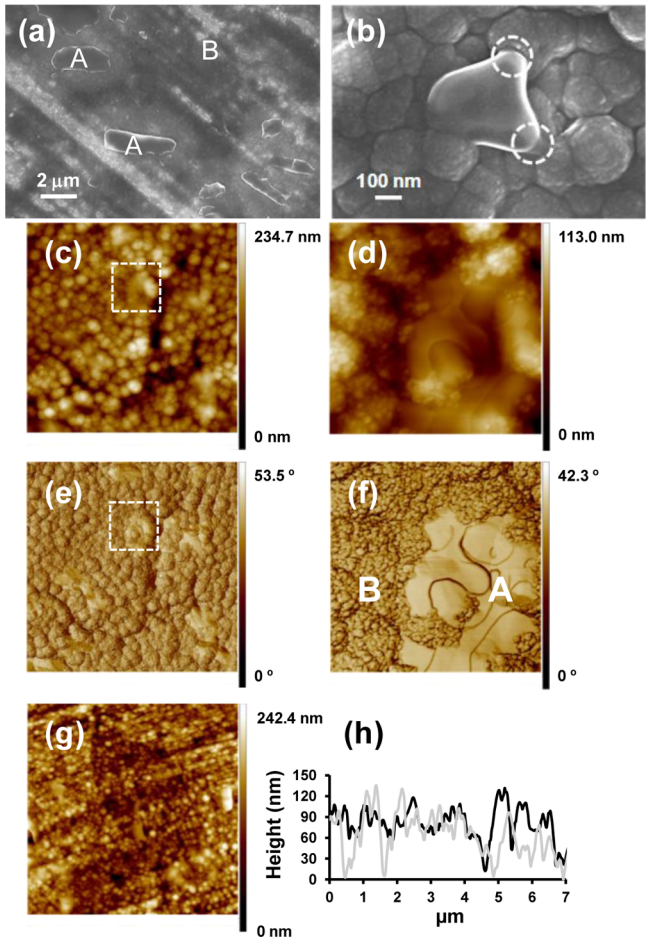

Figure 6. PNMPy−Omp2a surface characterization: (a) low- and (b) high-magnification SEM micrographs; (c) 5.0 × 5.0 μm and (d) 1.0 × 1.0 μm AFM height images; (e) 5 × 5 μm and (f) 1.0 × 1.0 μm AFM phase images corresponding to images c and d, respectively; (g) 10.0 × 10.0 μm AFM height image; and (h) cross-sectional profiles obtained from image c. Dashed circles in image b illustrate the connection between PNMPy and Omp2a particles. Squares in images c and e indicate the regions displayed in images d and f, respectively. Labels A and B in image f indicate the PNMPy and Omp2a phase, respectively. In the cross-sectional profiles, the black line corresponds to the diagonal drawn from the lower left corner to the upper right corner, while the gray line corresponds to the diagonal drawn from the upper left corner to the lower right corner.

submicrometric and micrometric dimensions with very homogeneous and smooth texture, and without the nodular outcrops typically found in PNMPy aggregates. These particles correspond to folded protein molecules, as evidenced by comparison with SEM micrographs derived from dialyzed Omp2a solutions (Supporting Information).

Although PNMPy and Omp2a proteins are interconnected in the composite (Figure 6b), well-defined morphological and texture differences reveal a complete phase separation. The latter fact is corroborated by the high contrasts observed in

DOI: 10.1021/am507142f
ACS Appl. Mater. Interfaces 2015, 7, 1632−1643

AFM phase images, which enable us to distinguish between the two phases in the composite. The smooth areas in Figure 6f (labeled A) correspond to the Omp2a phase, whereas the rough and irregular areas (labeled B) represent the PNMPy phase. The mean RMS roughness, which was measured considering several 5 × 5 μm windows, increases to 31 ± 5 nm upon the incorporation of the Omp2a protein.

Overall, morphological and topographical observations reveal that Omp2a proteins are well-distributed throughout the PNMPy-OMP2a composite surface, thus establishing pore structures. Although the PNMPy phase is characterized by a dense and compact matrix, MP functionality is expected to enhance the passive ion transport across the artificial membrane creating permanent ion channels.

Furthermore, contact angle measurements indicate that the surface of both steel (θ = 74° ± 7°) and PNMPy (θ = 67° ± 4°) shows some hydrophilicity, while PNMPy−Omp2a water-wettability increases significantly upon the incorporation of the MP (θ = 32° ± 8°). This effect is noticeably more pronounced for PNMPy−Omp2a than for composites prepared using PNMPy and other proteins (Supporting Information), as for example bovine serum albumin (BSA). This indicates that not only is Omp2a immobilized on the CP matrix, but it retains its natural disposition where the protein hydrophilic regions are positioned toward the outer region of the membrane, just as in biological environments. Although the isoelectric point of BSA (4.7) is very similar to that of Omp2a (4.5),[46] the contact angle value for PNMPy−BSA films prepared under similar experimental conditions (θ = 54° ± 7°) represents a reduction of only 20% with respect to PNMPy.

Electrochemical Properties. Cyclic voltammetry studies were run to determine the influence of these new formed ion channels in the electrochemical properties of the PNMPy−Omp2a composite. First, as occurred for the monomer (Supporting Information), the anodic process at around ∼1.1 V is less marked for PNMPy−Omp2a than for PNMPy (Figure 7). The ability to exchange charge reversibly, hereafter denoted electroactivity, increases with the similarity between the anodic and cathodic areas of the first control voltammogram. Thus, the electroactivity of PNMPy−Omp2a is 10% higher than that of PNMPy. This result, which is practically independent of the scan rate (Supporting Information), evidences the role played by the pore-forming protein in maintaining a flow of ions in and out of the CP matrix.

Besides, the electrochemically induced reduction of the thickness has been used to evaluate the relative porosity (Por) of PNMPy−Omp2a and PNMPy systems. Specifically, Por (in %) has been estimated as the difference between the thicknesses of the films as prepared and after 15 consecutive redox cycles (193 nm ±51 and 253 nm ±93 nm for PNMPy−Omp2a and PNMPy, respectively) relative to the thickness of the as-prepared film. The values obtained for Por are very similar for the two systems (i.e., 12 and 15%, respectively). Therefore, the difference observed in electroactivity and LEA values between PNMPy and PNMPy−Omp2a systems are mainly due to the operative state of Omp2a.

SEM micrographs recorded for PNMPy−Omp2a samples submitted to 15 redox cycles (Figure 8) reveal significant structural changes, which mainly affect the elements associated with the protein phase. Specifically, after a certain number of cycles, the smooth homogeneous particles (Figure 8a,b) disaggregate into a heterogeneous distribution of small spherical aggregates that have been associated with unfolded

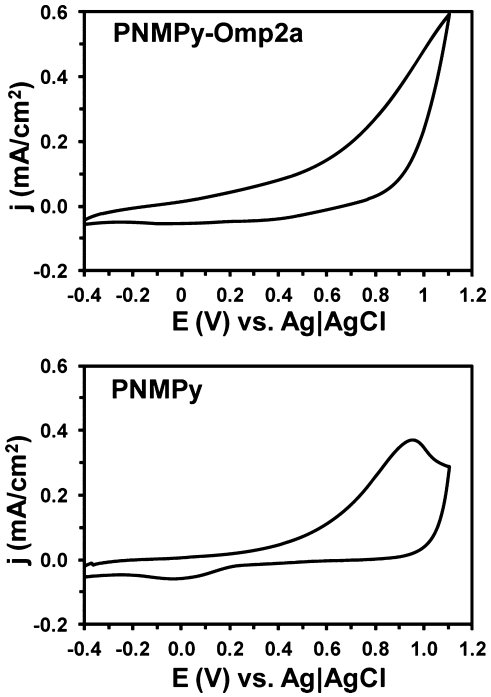

Figure 7. Cyclic voltammograms of PNMPy−Omp2a and PNMPy in aqueous solution with 0.1 M $LiClO_4$. Initial and final potentials, −0.40 V; reversal potential, 1.10 V; scan rate, 25 mV s^{-1}.

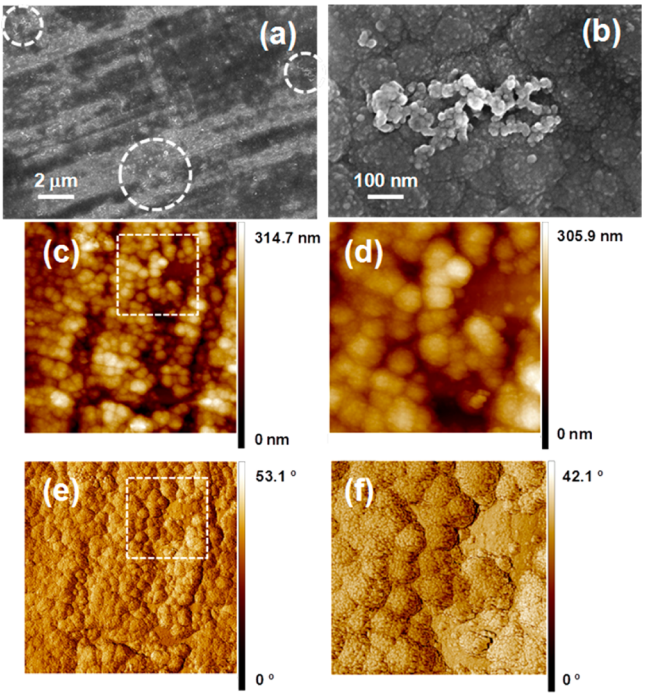

Figure 8. Surface characterization of PNMPy−Omp2a after 15 consecutive oxidation−reduction cycles: (a) Low and (b) high magnification SEM micrographs; (c) 5 × 5 μm and (d) 2.0 × 2.0 μm AFM height images; (e) 5 × 5 μm and (f) 2.0 × 2.0 μm AFM phase images corresponding to images c and e, respectively. Dashed circles in image a indicate the regions with unfolded protein. Squares in images c and e indicate the regions displayed in images d and f, respectively.

protein molecules. Accordingly, AFM images suggest that the 3D structure of the protein collapses, and only the space once

DOI: 10.1021/am507142f
ACS Appl. Mater. Interfaces 2015, 7, 1632−1643

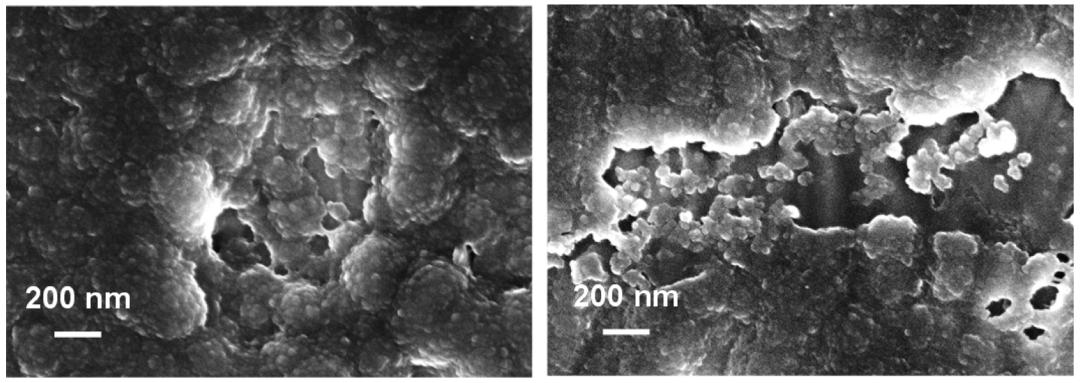

Figure 9. SEM micrographs for PNMPy−Omp2a composite after 72 h of immersion in a Lipase F-AP15 solution.

occupied by the Omp2a remains in the PNMPy surface. However, this aggressive electrochemically induced degradation process is not expected to occur when assessing the ion transport response of PNMPy−Omp2a by EIS because it is a nondestructive technique. Consequently, the functionality of the biomolecule in the composite is assured for passive ion transport applications (see below).

Biodegradability and Biocompatibility. CP-based platforms for biotechnological and biomedical applications typically require biodegradability and/or biocompatibility to minimize their impact on the environment and/or the adverse reaction of the body.[47] Accordingly, bearing those requirements in mind, and before performing EIS measurements, we conducted both enzymatic degradation and cell viability tests to validate the integrated-protein composite for bio-interface applications.

In the particular case of PNMPy−Omp2a, excessively rapid enzymatic degradation of the MP could greatly influence the applicability of the composite when used in physiological mediums. Consequently, the enzymatic biodegradability of Omp2a in the composite was investigated by monitoring the protein morphology change induced during 72 h of continuous immersion in a Lipase-containing solution. Samples extracted after 1, 4, 8, 24, and 72 h were observed by SEM, and results indicated severe degradation of the protein started after 24 h of immersion in the enzymatic solution (Supporting Information). Thus, the protein retained the initial aspect and texture in samples extracted after 1, 4, and 8 h. This feature suggests that the CP matrix protects Omp2a aggregates from the action of the enzyme at the earlier stages of degradation. Micrographs of samples extracted after 72 h revealed that the degraded protein is mostly detached from the surface of the films (Figure 9), indicating that the benefits provided by the protein to the composite are expected to be null after this time of exposure to aggressive bioconditions.

Quantitative results for cell adhesion assays are displayed in Figure 10a. The number of Vero and Cos-7 cells adhered to the surface of the PNMPy−Omp2a is significantly higher than that of PNMPy. This tendency is more evident in the case of Vero cells. On the other hand, the adhesion of both Vero and Cos-7 cells on the surface of PNMPy and PNMPy−Omp2a is favored with respect to the TCPS and Steel control substrates, which show similar relative viabilities.

On the other hand, SEM micrographs show the significant spreading of Cos-7 cells, which form cellular monolayers on the surface of PNMPy−Omp2a (Figure 10b), whereas large domains without cells appear on the surface of PNMPy (Figure 10c). The actin filaments emerging from the cells and with the

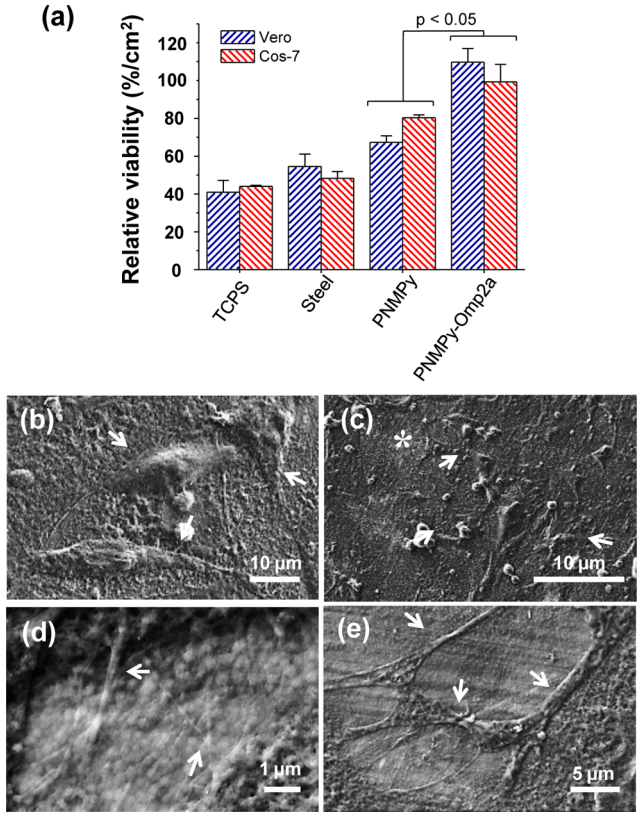

Figure 10. (a) Cellular adhesion onto PNMPy−Omp2a, PNMPy and steel surfaces using Vero (epithelial-like) and Cos-7 (fibroblast-like) cells. The relative viability was established in relation to the TCPS control (tissue culture polystyrene). ANOVA-Tukey test, $p < 0.05$. SEM micrographs of Cos-7 cells seeded for 24 h onto (b) PNMPy−Omp2a and (c) PNMPy surfaces. The asterisk in image c indicates substrate surface, while arrows in images b and c indicate the cells adhered onto the surface. Micrographs showing cellular interactions (arrows) at cultured PNMPy−Omp2a films: (d) connection sites (filopodia) between Cos-7 cells and the substrate and (e) intercellular junctions used for cell−cell communication processes.

barbed ends oriented toward the surface of PNMPy−Omp2a (Figure 10d), which are known as filopodia, are responsible for local adhesion. The grouping of these filaments results in stress fibers, denoted lamellipodia, that are used by cells to move along the substrate. Figure 10e shows typical connections between two Cos-7 cells to establish communication, which is a crucial step in the coordination of differentiation processes in eukaryotic cells. Similar features for cultured Vero cells are

DOI: 10.1021/am507142f
ACS Appl. Mater. Interfaces 2015, 7, 1632−1643

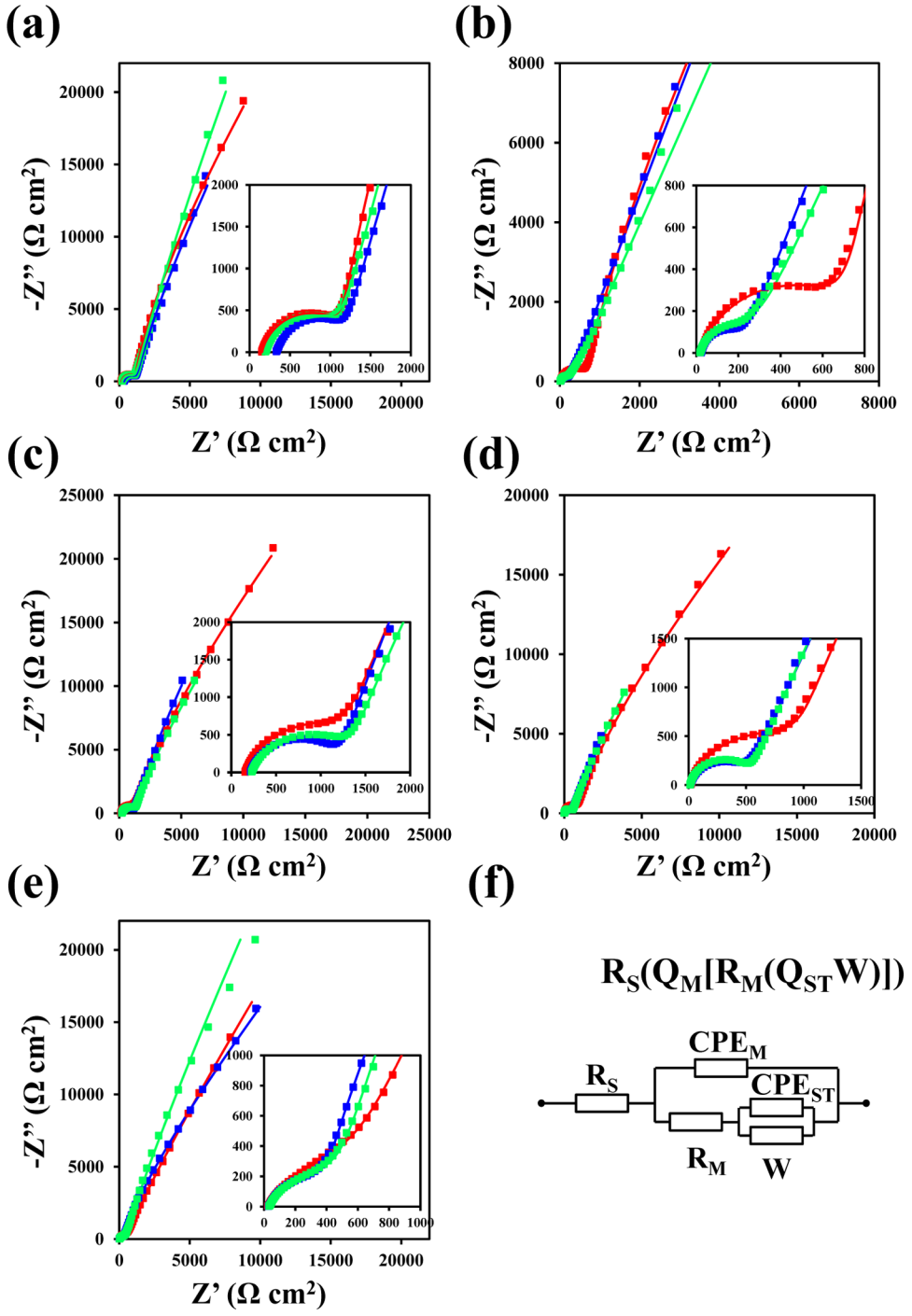

Figure 11. Nyquist plots for (red) PNMPy and (blue and green) PNMPy−Omp2a in an aqueous solution containing (a) 5 mM K^+, (b) 100 mM K^+, (c) 5 mM Na^+, (d) 140 mM Na^+, and (e) 5 mM K^+ + 140 mM Na^+. (f) Electrical equivalent circuit (EEC) used for fitting experimental data for PNMPy and PNMPy−Omp2a. R_S is the electrolyte resistance, CPE_M and R_M are the membrane constant phase element and resistance, respectively, CPE_{ST} is the steel constant phase element, and, W is the Warburg impedance.

displayed in the Supporting Information. Overall, the results presented in this section indicate that PNMPy−Omp2a is a potential candidate for biotechnological and biomedical applications in which biocompatibility is a requisite.

Ion Channels. EIS measurements have been carried out to evaluate the proper function of ion channels and pores formed by the MP in the PNMPy−Omp2a composite.[48−52] This methodology provides information not only of the ion transport but also a complete description of the investigated system, as was recently discussed in a comparative study.[53] Impedance was measured as a function of frequency for steel-supported PNMPy and PNMPy−Omp2a films. EIS spectra were registered using different aqueous electrolyte mediums: 5 and 100 mM KCl solutions and 5 and 140 mM NaCl solutions. It should be noted that Na^+ and K^+ are two main blood electrolytes, their normal blood levels being 135−145 and 3.5−5.2 mM, respectively. Moreover, the concentration of K^+ is 2 orders of magnitude higher in intracellular regions than outside the membrane, while the opposite occurs for Na^+.

DOI: 10.1021/am507142f
ACS Appl. Mater. Interfaces 2015, 7, 1632−1643

Table 2. Fitting Parameters Used to Simulate the EIS Spectra Using the Electrical Equivalent Circuit[a]

	PNMPy				PNMPy−Omp2a			
	5 mM K^+	100 mM K^+	5 mM Na^+	140 mM Na^+	5 mM K^+	100 mM K^+	5 mM Na^+	140 mM Na^+
R_S (Ω cm^2)	154 (0.2)	21.2 (1.0)	156 (0.4)	19.1 (1.0)	336 (0.4)	22.1 (0.6)	217 (0.3)	14.7 (0.7)
					201 (0.4)	18.2 (1.3)	229 (0.2)	14.5 (0.6)
R_M (Ω cm^2)	1158 (0.7)	821 (2.5)	1553 (1.7)	1249 (3.6)	1005 (0.6)	243 (2.1)	1096 (0.8)	589 (1.7)
					1074 (1.4)	328 (4.3)	1282 (0.6)	589 (1.3)
$Q_M \times 10^5$ (F cm^{-2} s^{n-1})	3.749 (1.6)	5.158 (4.5)	4.732 (2.5)	5.137 (4.4)	4.941 (3.7)	3.683 (5.5)	3.964 (2.0)	4.853 (3.1)
					3.788 (3.3)	5.906 (7.9)	5.006 (1.3)	2.886 (2.8)
n	0.8500 (0.3)	0.8254 (0.8)	0.8497 (0.5)	0.8597 (0.8)	0.8291 (0.9)	0.8884 (0.9)	0.8460 (0.5)	0.8494 (0.5)
					0.8363 (0.7)	0.8363 (0.7)	0.8161 (0.3)	0.8931 (0.4)
$Q_S \times 10^4$ (F cm^{-2} s^{n-1})	3.787 (0.6)	4.229 (2.7)	2.227 (1.3)	2.441 (4.0)	5.406 (1.2)	4.844 (0.7)	7.385 (0.9)	7.790 (3.4)
					4.013 (1.4)	4.533 (1.4)	5.852 (0.6)	5.580 (2.5)
n	0.9787 (0.5)	0.9579 (2.2)	0.9740 (1.2)	0.9869 (3.3)	0.9017 (1.3)	0.7626 (0.4)	0.8921 (1.0)	0.8169 (2.3)
					0.8720 (1.1)	0.7286 (0.8)	0.9292 (0.7)	0.8628 (1.7)
W $\times 10^5$ (Ω cm^2)	9.356 (2.6)	9.579 (12.5)	10.76 (2.9)	13.89 (7.2)	9.040 (8.9)	2.369 (0.89)	12.16 (7.8)	10.37 (19.5)
					3.626 (17.2)	1.630 (5.7)	17.39 (2.7)	13.77 (11.1)

[a]EIS spectra are displayed in Figure 11a−d, and electrical equivalent circuit is represented in Figure 11f. For PNMPy−Omp2a, the first and second values provided for each element correspond to the blue and green spectra, respectively. The error percentage associated to each circuit element is included in parentheses. Fitting parameters used to simulate the EIS spectra displayed in Figure 11e are listed in the Supporting Information.

Figure 11a−e compares representative Nyquist plots obtained for PNMPy and PNMPy−Omp2a in different Na^+- and/or K^+-containing media. In all cases, Nyquist spectra show a semicircle in the high-frequency range and a straight ascending line in the low-frequency range. The electrical equivalent circuit (EEC) used to fit the experimental data is shown in Figure 11f, where R_S corresponds to the electrolyte solution resistance and R_M represents the ability of the PNMPy−Omp2a system to impede ion transport at the interface between the electrolyte and the membrane. The ECC also includes double layer capacitances from both the membrane and steel (Q_M and Q_{ST}, respectively) and a Warburg impedance element (W), corresponding to the diffusion of water molecules. Therefore, both R_M and Q_M are associated with the overall contribution of the protein-integrated interface. It should be noted that the incorporation of ion channels through the immobilization of the MP is expected to alter the membrane resistance value, R_M. Accordingly, channel activity can be monitored by comparing the membrane resistance of PNMPy and PNMPy−Omp2a in the different media.

Table 2 lists the contribution of each element for PNMPy and PNMPy−Omp2a. Both capacitances were replaced by a constant phase element (CPE) that describes a nonideal capacitor when the phase angle is different from −90°. The CPE impedance is attributed to the surface reactivity, surface heterogeneity and roughness, which in turn are related to the electrode geometry and porosity. Also, the CPE impedance accounts for the nonuniform diffusion among the films adhered to the electrode surface. The CPE impedance, which has been expressed as $Z_{CPE} = [Q\ (j\omega)^n]^{-1}$, represents an ideal capacitor and a pure resistor for $n = 1$ and $n = 0$, respectively, while it is associated with a diffusion process when $n = 0.5$. The fitting quality was judged based on the error percentage associated with each circuit component, showing errors lower than 5% in most of the elements.

EIS results evidence that the pore-forming MP is properly immobilized in the PNMPy matrix, retaining the functionality associated with the β-barrel structure. More specifically, the response of PNMPy and PNMPy−Omp2 films is very similar for both the 5 mM K^+ and the 5 mM Na^+ electrolytic media (Figure 11a,c). Accordingly, the R_M values (Table 2), which indicate the facility to exchange ions between the system and the electrolyte solution, are very similar for the control PNMPy and the MP-containing composite. Similarly, the ability to store electrical charge and the diffusion impedance of PNMPy, which are defined by Q_M and W, respectively, are not significantly affected by the incorporation of the protein when the concentration of ions is low. In spite of this, the diffusion of hydrated Na^+ is slightly higher for the MP-composite than for the CP, suggesting that Omp2a is more efficient for the transport of Na^+ than for K^+.

In contrast, R_M values are lower for PNMPy−Omp2a than for PNMPy in the 100 mM K^+ and 140 mM Na^+ solutions (Figure 11b,d). Accordingly, PNMPy−Omp2a promotes the passive ion transport in solutions with high ionic concentrations, thus the MP functionality is enhanced when the concentration of ions in the medium is high. EIS spectra recorded in a solution containing 5 mM K^+ and 140 mM Na^+, which correspond to the concentrations of such ions in blood, evidence a similar behavior (Figure 11e). Thus, the ion transport resistance of PNMPy (1037 Ω cm^2) decreases 1 order of magnitude when the MP is immobilized in the PNMPy−Omp2a composite (~600 Ω cm^2), which activates the transport of ions.

Inspection of the Q_M values obtained for the 100 mM K^+ and 140 mM Na^+ solutions indicates that, as occurred for the solutions with lower concentrations of ions, the MP does not alter significantly the ability to store charge of the CP. Indeed, inspection of results displayed in Table 2 evidence that such ability is intrinsic to PNMPy because it is practically independent of the concentration and nature of the ions as well as of the Omp2a presence. Comparison of the diffusional impedance values obtained for more concentrated solutions also suggest that Omp2a favors the diffusion of hydrated Na^+ with respect to that of hydrated K^+. Thus, results for PNMPy indicate that the bulk diffusion of ions through the CP pores is practically independent of both the concentration and nature of ions. Accordingly, although ions affect the R_M of PNMPy, the diffusional activity of this material is not selective. In contrast, the impedance behavior observed for PNMPy−Omp2a

DOI: 10.1021/am507142f
ACS Appl. Mater. Interfaces 2015, 7, 1632−1643

evidence that R_M is very sensitive to the ions concentration, while W is affected by the nature of the ions. These features indicate that the MP brings not only ion transport capacity but also sensitivity and selectivity to the CP.

With this work, we have successfully produced a protein-integrated system that preserves the native structure and functionality of the MP. The combination of biological elements with synthetic materials is a challenging research field that requires further understanding of interactions and compatibility between materials. However, as a first step, PNMPy−Omp2a approach has resulted in a bio-interface with proven passive ion transport. Interestingly, as Omp2a allows the passive transport of other molecules such as nutrients and antibiotics, PNMPy−Omp2a composite can also be exploited to design bio-hybrid materials with multifunctional artificial channels for bio-applications.

CONCLUSIONS

In this work, novel CP−MP biocomposites have been prepared using PNMPy, which shows a very compact structure, and Omp2a from *Brucella melitensis*, a β-barrel protein that forms trimeric pores. The MP has been successfully immobilized onto the surface of PNMPy during the electrochemical polymerization, which has been proven by XPS and UV−vis spectroscopy analyses. Furthermore, Omp2a retained its native-state β-sheet structure, thus preserving its folded operative form. SEM and AFM characterization techniques enabled us to identify the PNMPy−Omp2a composite surface properties, which are related to the passive ion transport. As a result, Omp2a pore-forming structures are distributed throughout the compact PNMPy matrix. Additionally, PNMPy−Omp2a biocomposites are hydrophilic, electroactive, and biocompatible bio-interfaces.

Although the porosity of PNMPy and PNMPy−Omp2a are very similar, their responses toward electrolyte solutions are completely different. Thus, the behavior of PNMPy is independent of the electrolyte concentration, while PNMPy−Omp2a promotes the exchange of ions between the systems and the electrolyte solution. This passive transport ability, which is associated with the β-barrel structure of the immobilized protein, is regulated by the concentration of ions in the electrolyte solution.

PNMPy−Omp2a behaves as a smart bioinspired ion-channel, which has potential applications in different areas of the biomedical field, such as nanofluidics, energy conversion and biosensoring. Furthermore, changing the concentration of ions in the electrolyte solution regulates the activity of Omp2a nanochannels integrated in the PNMPy−Omp2a composite. This has been proved by examining the ion transport process using K^+ and Na^+ concentrations around those typically found in blood. Furthermore, results suggest that Omp2a is more efficient for the diffusion of Na^+ than for the diffusion of K^+. In addition to the above-mentioned applications, Omp2a immobilized onto PNMPy can be used to simulate the process of ions and small molecules transport in living organisms, enabling the investigation of the chemistry, size, and conformational states of β-barrel nanochannels.

ASSOCIATED CONTENT

Supporting Information

Sequence of the Omp2a protein, high resolution XPS spectra and assignment of the peaks, control voltammograms of monomer solutions, SEM micrographs of SDS and Omp2a, contact angles, cyclic voltammograms of PNMPy−Omp2a and PNMPy in aqueous solution with $LiClO_4$, SEM micrographs for PNMPy−Omp2a after 8 and 24 h of immersion in a Lipase F-AP15 solution, SEM micrographs of Vero and Cos-7 cells seeded for 24 h onto steel, and SEM micrographs of Vero cells seeded for 24 h onto PNMPy and PNMPy−Omp2a surfaces. This material is available free of charge via the Internet at http://pubs.acs.org

AUTHOR INFORMATION

Corresponding Author

*E-mail: carlos.aleman@upc.edu.

Notes

The authors declare no competing financial interest.

ACKNOWLEDGMENTS

Financial support from the MINECO and FEDER (MAT2012-34498) and the Generalitat de Catalunya (2014SGR254 and XRQTC) is gratefully acknowledged. M.M.P.-M. thanks financial support through an FPI-UPC grant. C.M. and E.A.P. thank the Belgian National Fund for Scientific Research for their research associate and senior research associate positions, respectively. Support for the research of C.A. was received through the ICREA Academia prize for excellence in research funded by the Generalitat de Catalunya.

REFERENCES

(1) Li, C.; Bai, H.; Shi, G. Conducting Polymer Nanomaterials: Electrosynthesis and Applications. *Chem. Soc. Rev.* **2009**, *38*, 2397−2409.

(2) Coelho, E. C. S.; Nascirnento, V. B.; Ribeiro, A. S.; Navarro, M. Electrochemical and Optical Properties of New Electrochromic and Fluorescent Nitrobenzoyl Polypyrrole Derivatives. *Electrochim. Acta* **2014**, *123*, 441−449.

(3) Longa, Y.-Z.; Lia, M.-M.; Gub, C.; Wanc, M.; Duvaild, J.-L.; Liue, Z.; Fanf, Z. Recent Advances in Synthesis, Physical Properties, and Applications of Conducting Polymer Nanotubes and Nanofibers. *Prog. Polym. Sci.* **2011**, *36*, 1415−1442.

(4) Guo, B.; Glavas, L.; Albertsson, A.-C. Biodegradable and Electrically Conducting Polymers for Biomedical Applications. *Prog. Polym. Sci.* **2013**, *38*, 1263−1338.

(5) Romero, I. S.; Schurr, M. L.; Lally, J. V.; Kotlik, M. Z.; Murphy, A. R. Enhancing the Interface in Silk−Polypyrrole Composites through Chemical Modification of Silk Fibroin. *ACS Appl. Mater. Interfaces* **2013**, *5*, 553−564.

(6) Martí, M.; Fabregat, G.; Estrany, F.; Alemań, C.; Armelin, E. Nanostructured Conducting Polymer for Dopamine Detection. *J. Mater. Chem.* **2010**, *20*, 10652−10660.

(7) Bongo, M.; Winther-Jensen, O.; Himmelberger, S.; Straskosas, X.; Ramuz, M.; Hama, A.; Stavrinidou, E.; Malliaras, G. G.; Salleo, A.; Winther-Jensen, B.; Owens, R. M. PEDOT:Gelatin Composites Mediate Brain Endothelial Cell Adhesion. *J. Mater. Chem. B* **2013**, *1*, 3860−867.

(8) Hassanien, R.; Al-Hinai, M.; Al-Said, S. A. F.; Little, R.; Siller, L.; Wright, N. G.; Houlton, A.; Horrocks, B. R. Preparation and Characterization of Conductive and Photoluminescent DNA Templated Polyindole Nanowires. *ACS Nano* **2010**, *4*, 2149−2159.

(9) Ma, Y.; Chiu, P. L.; Serrano, A.; Ali, S. R.; Chen, A. M.; He, H. The Electronic Role of DNA-Functionalized Carbon Nanotubes: Efficacy for in Situ Polymerization of Conducting Polymer Nanocomposites. *J. Am. Chem. Soc.* **2008**, *130*, 7921−7928.

(10) Romero, I. S.; Bradshaw, N. P.; Larson, J. D.; Severt, S. Y.; Roberts, S. J.; Schiller, M. L.; Leger, J. M.; Murphy, A. R. Biocompatible Electromechanical Actuators Composed of Silk-Conducting Polymer Composites. *Adv. Funct. Mater.* **2014**, *24*, 3866−3875.

DOI: 10.1021/am507142f
ACS Appl. Mater. Interfaces 2015, 7, 1632−1643

(11) Taraska, J. W. Mapping Membrane Protein Structure with Fluorescence. *Curr. Opin. Struct. Biol.* **2012**, *22*, 507−513.
(12) Barrera, N. P.; Zhou, M.; Robinson, C. V. The Role of Lipids in Defining Membrane Protein Interactions: Insights from Mass Spectrometry. *Trends Cell Biol.* **2013**, *23*, 1−46.
(13) Stora, T.; Lakey, J. H.; Vogel, H. Ion-Channel Gating in Transmembrane Receptor Proteins: Functional Activity in Tethered Lipid Membranes. *Angew. Chem., Int. Ed.* **1999**, *38*, 389−392.
(14) Bowie, J. U. Solving the Membrane Protein Folding Problem. *Nature* **2005**, *438*, 581−589.
(15) Jungbauer, A.; Kaar, W. Current Status of Technical Protein Refolding. *J. Biotechnol.* **2007**, *128*, 587−596.
(16) Valiokas, R.; Vaitekonis, S.; Klenkar, G.; Trinkūnas, G.; Liedberg, B. Selective Recruitment of Membrane Protein Complexes onto Gold Substrates Patterned by Dip-Pen Nanolithography. *Langmuir* **2006**, *22*, 3456−3460.
(17) Kumar, M.; Habel, J. E. O.; Shen, Y.-X.; Meier, W. P.; Walz, T. High-Density Reconstitution of Functional Water Channels into Vesicular and Planar Block Copolymer Membranes. *J. Am. Chem. Soc.* **2012**, *134*, 18631−18637.
(18) Kita-Tokarczyk, K.; Grumelard, J.; Haefele, T.; Meier, W. Block Copolymer Vesicles—Using Concepts from Polymer Chemistry to Mimic Biomembranes. *Polymer* **2005**, *46*, 3540−3563.
(19) González-Pérez, A.; Stibius, K. B.; Vissing, T.; Nielsen, C. H.; Mouritsen, O. G. Biomimetic Triblock Copolymer Membrane Arrays: A Stable Template for Functional Membrane Proteins. *Langmuir* **2009**, *25*, 10447−10550.
(20) Graff, A.; Sauer, M.; Van Gelder, P.; Meier, W. Virus-Assisted Loading of Polymer Nanocontainer. *Proc. Natl. Acad. Sci. U.S.A.* **2002**, *99*, 5064−5068.
(21) Yao, K.; Liu, C.; Chen, Y.; Chen, L.; Li, F.; Liu, K.; Sun, R.; Wang, P.; Yang, C. Integration of Light-Harvesting Complexes into the Polymer Bulk Heterojunction. *J. Mater. Chem.* **2012**, *22*, 7342−7349.
(22) Shen, Y.-X.; Saboe, P. O.; Sines, I. T.; Erbakan, M.; Kumar, M. Biomimetic Membranes: A Review. *J. Membr. Sci.* **2014**, *454*, 359−381.
(23) Mecke, A.; Dittrich, C.; Meier, W. Biomimetic Membranes Designed from Amphiphilic Block Copolymers. *Soft Matter* **2006**, *2*, 751−759.
(24) Arun, N.; Narayan, K. S. Conducting Polymers as Antennas for Probing Biophysical Activities. *J. Phys. Chem. B* **2008**, *112*, 1564−1569.
(25) Della Pia, E. A.; Holm, J. V.; Lloret, N.; Le Bon, C.; Popot, J.-L.; Zoonens, M.; Nygård, J.; Martinez, K. L. A Step Closer to Membrane Protein Multiplexed Nanoarrays Using Biotin-Doped Polypyrrole. *ACS Nano* **2014**, *8*, 1844−1853.
(26) Boschiroli, M.-L.; Foulongne, V.; O'Callaghan, D. A Worldwide Zoonosis. *Curr. Opin. Microbiol.* **2001**, *4*, 58−64.
(27) Paquet, J.-Y.; Diaz, M. A.; Genevrois, S.; Grayon, M.; Verger, J.-M.; De Bolle, X.; Lakey, J. H.; Letesson, J.-J.; Cloeckaert, A. Molecular, Antigenic, and Functional Analyses of Omp2b Porin Size Variants of *Brucella* spp. *J. Bacteriol.* **2001**, *183*, 4839−4847.
(28) Roussel, G.; Matagne, A.; De Bolle, X.; Perpète, E.; Michaux, C. Purification, Refolding, and Characterization of the Trimeric Omp2a Outer Membrane Porin from *Brucella melitensis*. *Protein Expression Purif.* **2012**, *83*, 198−204.
(29) Roussel, G.; Perpète, E. A.; Tinti, E.; Michaux, C. Towards a Universal Method for Protein Refolding: The Trimeric Beta Barrel Membrane Omp2a as a Test Case. *Biotechnol. Bioeng.* **2013**, *110*, 417−423.
(30) Aradilla, D.; Estrany, F.; Alemán, C. Symmetric Supercapacitors based on Multilayers of Conducting Polymers. *J. Phys. Chem. C* **2011**, *115*, 8430−8438.
(31) Aradilla, D.; Estrany, F.; Armelin, E.; Alemán, C. Morphology and Growing of Nanometric Multilayered Films Formed by Alternated Layers of Poly(3,4-ethylenedioxythiophene) and Poly(*N*-methylpyrrole). *Thin Solid Films* **2010**, *518*, 4203−4210.
(32) McQuade, D. T.; Pullen, A. E.; Swager, T. M. Conjugated Polymer-Based Chemical Sensors. *Chem. Rev.* **2000**, *100*, 2537−2574.
(33) Teixeira-Dias, B.; Alemán, C.; Estrany, F.; Azambuja, D. S.; Armelin, E. Microstructures of Poly(*N*-methylpyrrole) and Their Interaction with Morphine. *Electrochim. Acta* **2011**, *56*, 5836−5847.
(34) Anwar, N.; Vagin, M.; Laffir, F.; Armstrong, G.; Dickinson, C.; McCormac, T. Transition Metal Ion-Substituted Polyoxometalates Entrapped in Polypyrrole as an Electrochemical Sensor for Hydrogen Peroxide. *Analyst* **2012**, *137*, 624−630.
(35) Bendrea, A.-D.; Fabregat, G.; Cianga, L.; Estrany, F.; del Valle, L. J.; Cianga, I.; Alemán, C. Hybrid Materials Consisting of an All-Conjugated Polythiophene Backbone and Grafted Hydrophilic Poly(ethylene glycol) Chains. *Polym. Chem.* **2013**, *4*, 2709−2723.
(36) Fabregat, G.; Alemán, C.; Casas, M. T.; Armelin, E. Controlling the Morphology of Poly(*N*-cyanoethylpyrrole). *J. Phys. Chem. B* **2012**, *116*, 5064−5070.
(37) Eby, D. M.; Artyushkova, K.; Paravastu, A. K.; Johnson, G. R. Probing the Molecular Structure of Antimicrobial Peptide-Mediated Silica Condensation Using X-ray Photoelectron Spectroscopy. *J. Mater. Chem.* **2012**, *22*, 9875−9883.
(38) Stevens, J. S.; de Luca, A. C.; Pelendritis, M.; Terenghi, G.; Downes, S.; Schroeder, S. L. M. Quantitative Analysis of Complex Amino Acids and RGD Peptides by X-ray Photoelectron Spectroscopy (XPS). *Surf. Interface Anal.* **2013**, *45*, 1238−1246.
(39) Cioffi, N.; Torsi, L.; Losito, I.; Di Franco, C.; De Bari, I.; Chiavarone, L.; Scamarcio, G.; Tsakova, V.; Sabbatini, L.; Zambonin, P. G. Electrosynthesis and Analytical Characterisationof Polypyrrole Thin Films Modified with Copper Nanoparticles. *J. Mater. Chem.* **2001**, *11*, 1434−1440.
(40) Bhattacharyya, D.; Gleason, K. K. Single-Step Oxidative Chemical Vapor Deposition of −COOH Functional Conducting Copolymer and Immobilization of Biomolecule for Sensor Application. *Chem. Mater.* **2011**, *23*, 2600−2605.
(41) Tougaard, S. Surface Nanostructure Determination by X-Ray Photoemission Spectroscopy Peak Shape Analysis. *J. Vac. Sci. Technol. A* **1996**, *14*, 1415−1423.
(42) Naumkin, A. V.; Kraut-Vass, A.; Gaarenstroom, S. W.; Powell, C. J. NIST X-ray Photoelectron Spectroscopy Database, http://srdata.nist.gov/xps/XPSDetailPage.aspx?AllDataNo=21109 (accessed April, 2014).
(43) Schmid, F.-X. *Biological Macromolecules: UV−Visible Spectrophotometry*, In *Encyclopedia of Life Sciences*; John Wiley & Sons, Ltd.: New York, 2001.
(44) Venyaminov, S. Y.; Yang, J. T. In *Circular Dichroism and the Conformational Analysis of Biomolecules*, Fasman, G. D., Ed. Plenum Press: New York, 1996; pp 69−104.
(45) Meng, H.; Zheng, J.; Lovinger, A. J.; Wang, B.-C.; Van Patten, P. G.; Bao, Z. Oligofluorene−Thiophene Derivatives as High-Performance Semiconductors for Organic Thin Film Transistors. *Chem. Mater.* **2003**, *15*, 1778−1787.
(46) Ge, S.; Kojio, K.; Takahara, A.; Kajiyama, T. Bovine Serum Albumin Adsorption onto Immobilized Organotrichlorosilane Surface: Influence of the Phase Separation on Protein Adsorption Patterns. *J. Biomater. Sci. Polym. Ed.* **1998**, *9*, 131−150.
(47) Pérez-Madrigal, M. M.; Giannotti, M. I.; del Valle, L. J.; Franco, L.; Armelin, E.; Puiggalí, J.; Sanz, F.; Alemán, C. Thermoplastic Polyurethane:Polythiophene Nanomembranes for Biomedical and Biotechnological Applications. *ACS Appl. Mater. Interfaces* **2014**, *6*, 9719−9732.
(48) Lin, J.; Motylinski, J.; Krauson, A. J.; Wimley, W. C.; Searson, P. C.; Hristova, K. Interactions of Membrane Active Peptides with Planar Supported Bilayers: An Impedance Spectroscopy Study. *Langmuir* **2012**, *28*, 6088−6096.
(49) Silva, B. P. G.; de Florio, D. Z.; Brochsztain, S. Characterization of a Perylenediimide Self-Assembled Monolayer on Indium Tin Oxide Electrodes Using Electrochemical Impedance Spectroscopy. *J. Phys. Chem. C* **2014**, *118*, 4103−4112.
(50) Smeazzetto, S.; Sacconi, A.; Schwan, A. L.; Margheri, G.; Tadini-Buoninsegni, F. Binding of a Monoclonal Antibody to the Phospholamban Cytoplasmic Domain Interferes with the Channel

DOI: 10.1021/am507142f
ACS Appl. Mater. Interfaces 2015, 7, 1632−1643

Activity of Phospholamban Reconstituted in a Tethered Bilayer Lipid Membrane. *Langmuir* **2014**, *30*, 10384−10388.
(51) Valincius, G.; Meskauskas, T.; Ivanauskas, F. Electrochemical Impedance Spectroscopy of Tethered Bilayer Membranes. *Langmuir* **2012**, *28*, 977−990.
(52) de Groot, G. W.; Demarche, S.; Santonicola, M. G.; Tiefenauer, L.; Vancso, G. J. Smart Polymer Brush Nanostructures Guide the Self-Assembly of Pore-Spanning Lipid Bilayers with Integrated Membrane Proteins. *Nanoscale* **2014**, *4*, 2228−2237.
(53) Müller, F.; Ferreira, C. A.; Azambuja, D. S.; Alemán, C.; Armelin, E. A. Measuring the Proton Conductivity of Ion-Exchange Membranes Using Electrochemical Impedance Spectroscopy and Through-Plane Cell. *J. Phys. Chem. B* **2014**, *118*, 1102−1112.

DOI: 10.1021/am507142f
ACS Appl. Mater. Interfaces 2015, 7, 1632−1643